RSC Advances

PAPER

View Article Online
View Journal | View Issue

Cite this: *RSC Adv.*, 2025, **15**, 25103

Prioritization of phytochemical isolation and characterization against HER2 as a breast cancer target based on chromatographic methods, DFT studies, 3D-QSAR analysis, and molecular docking simulations†

B. S. Lakshmi,[a] Jayanna K. Bidarur,[a] H. G. Anilkumar[b] and B. S. Ravindranath *[c]

Cancer remains one of the leading causes of death globally. Over the past few decades, significant advancements in cancer diagnostics, prevention, and therapeutics have been achieved. However, developing effective treatments with minimal adverse effects remains the most critical challenge for the medical community. Breast cancer is the second most common cause of cancer-related death in women. Thus, there is a need for novel therapeutic strategies that can effectively cure cancer. In the present study, we extracted very efficient bioactive phytocompounds from the *Vitex negundo* plant species, which has shown abundant medicinal properties since ancient times. The extracted plant sample was isolated and purified using HPLC analysis and LC-MS techniques. The LC-MS studies revealed the presence of two important bioactive phytocompounds, artemetin and catechin, in the plant extract. The functional groups present in each phytochemical were evaluated by FTIR analysis. Quantitative Structure–Activity Relationship (QSAR) studies were performed to understand the structure–activity relationships of bioactive compounds virtually, thereby minimizing labor costs and time. Artemetin and Catechin extracted from plant samples were evaluated for their antioxidant activity and anticancer activity using *in silico* molecular docking studies. Further, the physicochemical properties of these phytocompounds were analyzed using density functional theory (DFT) studies. These results suggest the efficiency of the method used to isolate phytocompounds with target-specific activity.

Received 13th March 2025
Accepted 1st July 2025

DOI: 10.1039/d5ra01800e

rsc.li/rsc-advances

1 Introduction

Phytochemicals are natural chemicals available in nature.[1,2] For many years, these natural chemicals have been used as traditional medicines. Several secondary metabolites obtained from medicinal plants in the form of phytochemicals have been reported to have anticancer properties and have been administered as medications for centuries to treat various human ailments.[3–5] These phytochemicals extracted from plants are classified as phenolics, terpenoids, lipids, alkaloids, carbohydrates, and nitrogen-containing compounds depending on their chemical structures and properties.[6] Furthermore, these phenolics are classified as flavonoids and lignin compounds. *Vitex negundo* is one such plant, rich in diverse phytochemicals in all its parts.[7] *V. negundo* is a large aromatic shrub present in most of the tropical regions of the Indian sub-continent. It belongs to the Verbenaceae family and is also called the "chaste tree".[8] It is used as a traditional medicine in many regions of the Himalayas.[9] It is used as a medicine with many pharmacological activities such as anti-inflammatory, antioxidant, antimicrobial, diuretic, and analgesic effects, among others.[10,11]

According to GLOBOCAN estimates for 2022, the incidence of cancer reached 20 million new cases, and the mortality rate is approximately 9.7 million.[12] Among these, breast cancer, a frequent malignancy in women, accounts for 0.5 million of all cancer-related fatalities.[5] Even with significant improvements in breast cancer treatment, the mortality rate remains relatively high. The second most common cause of cancer-related deaths in women is breast cancer.[13]

Breast cancer is differentiated into three major types: the most common type is caused by the upregulation of estrogen receptors (ERs) or progesterone receptors (PRs) in about 60% cases. This is also called hormone-receptor-positive breast cancer.[14] The abnormal expression of human epidermal growth factor receptor 2 (HER-2) causes the second type, which

[a]*Department of Chemistry, B. N. M. Institute of Technology, Bengaluru – 560070, Karnataka, India*

[b]*Department of Science and Humanities, PES University, BSK III Stage, Bengaluru, 560085, Karnataka, India*

[c]*Department of Biotechnology, Manipal Institute of Technology, Manipal, Manipal Academy of Higher Education, Manipal-576104, Karnataka, India. E-mail: ravindranath.bs@manipal.edu*

† Electronic supplementary information (ESI) available. See DOI: https://doi.org/10.1039/d5ra01800e

comprises about 15–20% of cases. The last type is triple-negative breast cancer (TNBC), which is not caused by the overexpression of ERs, HER-2 or PRs. Chemotherapy for breast cancer primarily focuses on the activity of these receptors, as they are the cause of the initiation and progression of the disease. Endocrine therapy is utilized in treating hormone-receptor-positive (ER- or PR-positive) breast cancer. EGFR is significant in triple-negative breast cancer (TNBC).[15] An increased level of EGFR was shown by many TNBC cell lines,[16] therefore the usage of EGFR fractional expression can show whether a treatment strategy is working. The available medicines used for treating breast cancer, such as gefitinib,[17] erlotinib,[17] pertuzumab,[18] palbociclib,[18] raloxifene,[19] show comparatively high levels of adverse effects. Therefore, phytocompounds and their bioactive derivatives, due to their potential anticancer abilities, may serve as an alternative therapy for treating breast cancer.[20] To effectively treat breast cancer with minimal side effects, an alternative treatment must be developed.

In the current study, *V. negundo* plants were subjected to extraction, purification, isolation, and characterization for our investigation. Analytical techniques such as HPLC analysis,[21] LC-MS analysis,[22,23] density functional theory (DFT) studies,[24] and Quantitative Structure–Activity Relationship (QSAR) studies[25] were used to extract and study the phytochemicals artemetin and catechin for their antioxidant and anticancer activities, respectively. The chosen breast cancer target proteins were used in molecular docking experiments involving artemetin and catechin. Further clinical trials are needed to assess the full potential of the phytochemicals derived from *V. negundo*.

2 Experimental

2.1 Materials and methods

2.1.1 Collection of *Vitex negundo* plants. During the winter months of December through February, *V. negundo* plants were collected from the Sahyadri mountain range in the Shivamogga district of Karnataka. Botanists at Kuvempu University (http://www.kuvempu.ac.in/) authenticated the plants.

2.1.2 Sample preparation. The leaves of the *V. negundo* plants were gathered, cleaned with distilled water, and dried under shade for 15–20 days. Using a Soxhlet device, the powdered dry leaves were extracted with absolute ethanol. The extract was filtered and concentrated by solvent evaporation under reduced pressure or vacuum.[25] The final extract was further analyzed using HPLC,[21] LC-MS,[23] and FTIR.[27]

2.1.3 Instrumentation

2.1.3.1 HPLC analysis. A Shimadzu HPLC system (Shimadzu Nexera-i LC2040C 3D-PDA, Tokyo, Japan) was utilized for analyzing the plant extract of *V. negundo*. An autosampler, SIL HTA; pump, LC-10ADVp; degasser, DGU-12A; detector, SPD-10AVp; and column oven, CTO-10AVp, make up the Shimadzu HPLC system.[21] 100 mg of plant sample and 50 mL of ethanol were added to a conical flask. After 5–6 min of sonication of the plant sample and ethanol solvent in a water bath, the mixture was sieved through a 0.45 μm microporous filter. HPLC analysis was performed using a C18 column (3.5 μm particle size, 50 × 4.6 mm) to analytically separate phytocompounds from the sample. The elution process was performed using a mobile phase composed of 0.1% formic acid in a mixture of water and acetonitrile, while the flow rate was kept constant at 1.2 mL min^{-1}; additionally, twenty liters of sample volume were injected. An ultraviolet (UV) detector is utilized to monitor at wavelengths of 225 nm and 254 nm. The following gradient elution mode was applied in a solvent system containing stages A (0.1% formic acid) and B (acetonitrile): 75–15% (B) from 8.00–11.00 min; and 15–15% (B) for 11.00–15.00 min, 75–75% (B) from 6.00–8.00 min, and 15–75% (B) from 0.01–6.00 min. In addition, until analysis, the column's equilibrium was maintained at 15% (B).[26] HPLC chromatograms of *V. negundo* plant extract detected at 254 nm and 225 nm are shown in Fig. 1, and the details of HPLC peaks are provided in Table 1.

2.1.3.2 LC-MS analysis. WATERS XBridge apparatus[27] with dimensions of 50 × 4.6 mm and 3.5 μm size was used in the current investigation to conduct the LC-MS analysis. Utilizing

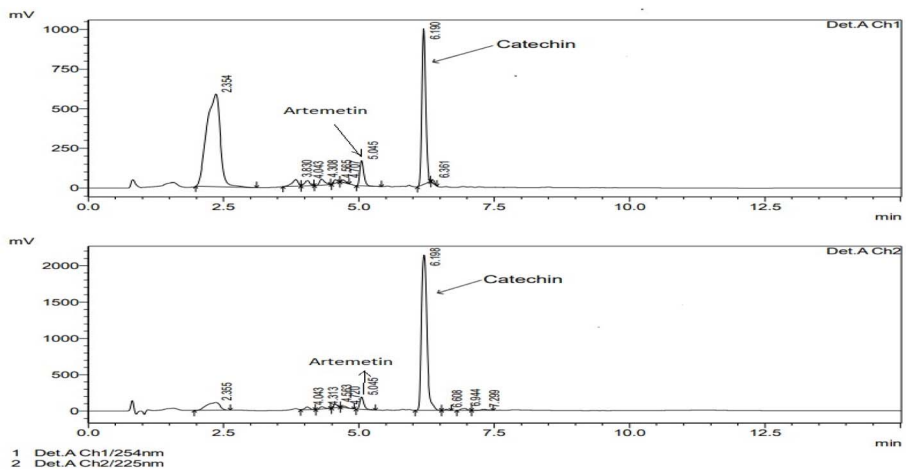

Fig. 1 HPLC chromatograms of *V. negundo* plant extract detected at 254 nm and 225 nm.

Table 1 Details of HPLC peaks of ethanol leaf extracts of *V. negundo*

Peak #	Ret. time	Area	Height	Area (%)
(A) Detected at 254 nm				
1	2.354	10 180 702	584 767	60.877
2	3.830	341 997	41 253	2.045
3	4.043	206 049	31 668	1.232
4	4.308	231 381	35 942	1.384
5	4.565	93 051	21 525	0.556
6	4.707	65 175	14 949	0.390
7	5.045	786 520	158 039	4.703
8	6.190	4 766 117	981 082	28.500
9	6.361	52 302	16 001	0.313
Total		16 723 294	1 885 227	100.000
(B) Detected at 225 nm				
1	2.355	1 827 556	107 363	9.758
2	4.043	230 077	37 487	1.228
3	4.313	215 694	34 052	1.152
4	4.563	240 264	54 139	1.283
5	4.720	114 105	21 300	0.609
6	5.045	844 791	169 481	4.511
7	6.198	14 887 679	2 134 910	79.492
8	6.608	55 557	12 523	0.297
9	6.944	202 881	25 917	1.083
10	7.299	109 815	13 917	0.586
Total		18 728 418	2 611 088	100.000

a C18 column, the sample was separated. The gradient was eluted at a steady flow rate of 1.2 mL min^{-1} using solvent A (distilled water diluted with 0.1% formic acid) and solvent B (acetonitrile, MS grade). The diluent mixture consists of TFA, methanol, acetonitrile, water, and 0.1% formic acid. During the whole 15 minute flow period, the temperature of the column remained at 30 °C. A volume of 20 μL of fluid was injected.[28] Electrospray mass spectra data were obtained in both positive and negative ionization modes, with a mass range of 50–1000 *m*/*z*. Waters MS spectroscopy was used with the Micromass Quattro Micro model and MassLynx software, version 4.1SCN805.[29] The MS condition maintained was triple quadrupole (QqQ) MSMS.[29] An electrospray ionization (ESI) source was used to record the mass spectrum for both ionization modes. A capillary voltage of 3.45 kV and collision gas flow desolvation of 800 L h^{-1} were used in both ion modes. We used the 50 L per h cone. The temperature source was kept at 110 °C for both ion modes, whereas the desolvation temperature was maintained at 350 °C. For both ionization modes, the energy of ionization I (0.50 eV) was kept constant. An ionization energy II of 3.0 eV is maintained during both ionization operations. Both of the ionization modes, which used the mass range of 100–1000 *m*/*z*, are coupled to the mass detector. An external device was utilized for further assessment.[22,23] As shown in Fig. 2, the major compounds from *V. negundo* were analysed using the LC-MS ES-TIC chromatogram at 254 nm. The LC-MS chromatograms of the phytochemicals artemetin and catechin extracted from *V. negundo* are shown in Fig. 3.

2.1.3.3 QSAR analysis. The structure-based virtual bioactive compound screening was carried out with minimal exertion and time usage, and a QSAR model was developed. Open3DQSAR,[30] Open3DALIGN,[31] PyMOL[32] and Discovery Studio Visualizer[33] related programs were combined to create the Cloud 3D-QSAR server.[34] This service enables us to quickly upload our own datasets and automatically carry out CoMFA modelling (comparative molecular field analysis), which covers all necessary stages, including molecular alignment and the computation of the MIF (molecular interaction field).[35] After the models are effectively developed, the server will deliver all necessary findings, which users can then analyse along with a forecasting function.

2.1.3.4 Molecular docking studies. Molecular docking simulations were performed to analyze the best orientations of the protein–ligand interactions of interest. The RCSB Protein Data Bank (PDB) database, which has higher-resolution PDB structures, was used to retrieve the selected protein structures in this study.[36] The molecular docking procedure employed phytochemicals that were chosen as phyto-ligands based on LC-MS investigations. The breast cancer protein targets were assessed through their binding affinities. The binding energies were calculated for each phytocompound. The instruments utilized to carry out the PDB formatting and ligand preparation processes include the PDB database,[37] MGL Tools,[38] AutoDock

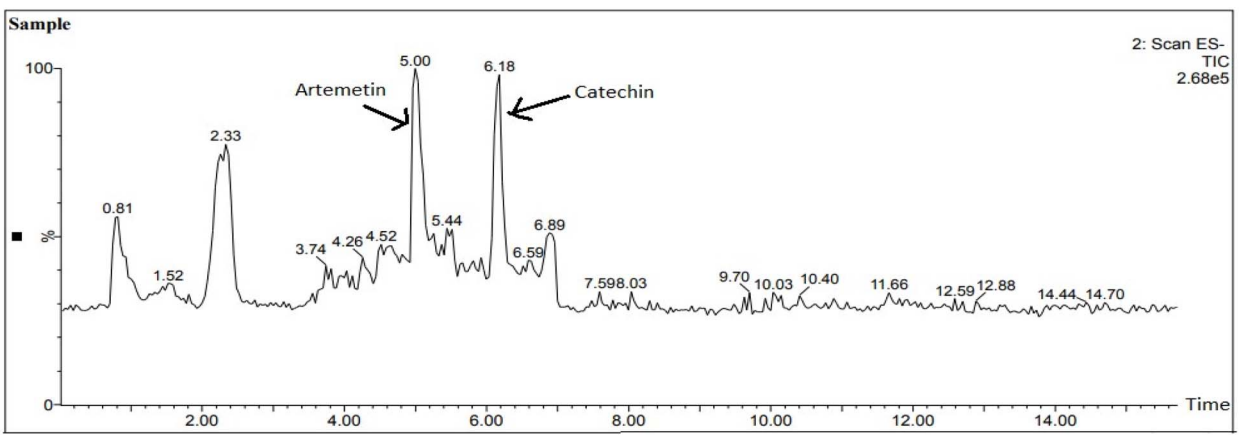

Fig. 2 The major compounds from *V. negundo*, analysed using LC-MS ES-TIC (254 nm).

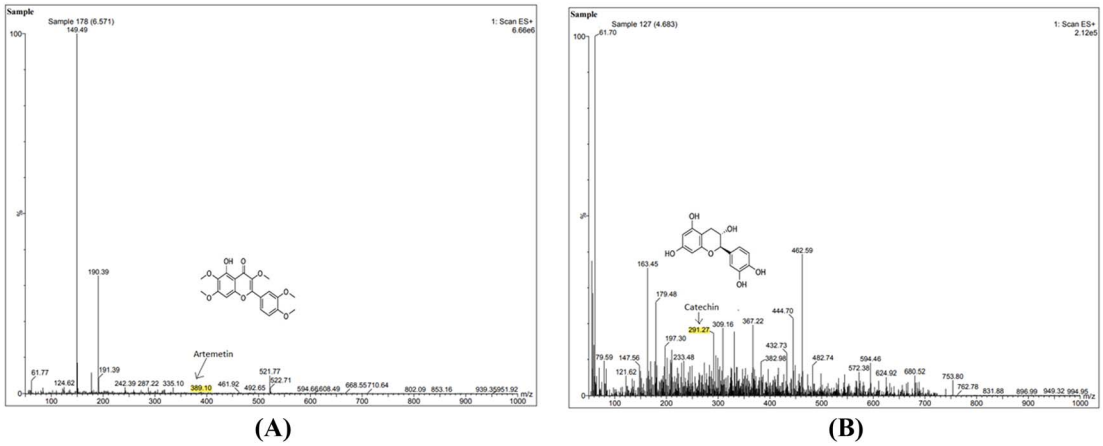

Fig. 3 LC-MS chromatograms of the phytochemicals (A) artemetin and (B) catechin extracted from *V. negundo*.

Vina,[39] PyRx,[40] Open Babel,[41] PyMol,[32] and Discovery Studio software.[33] The phytoligands were chosen based on LC-MS data and standard compounds were explored from the PubChem database[42] and converted to SDF formats.[45] The ligands were refined using Open Babel software[43] and moved to AutoDock Vina,[39] which is inbuilt into PyRx.[40,46,47] The results were evaluated using Discovery Studio Visualizer.[44]

2.1.3.5 FTIR analysis. FTIR (Fourier transform infrared)[48] transmission spectra of *V. negundo* leaf extracts were collected using an Alpha II Fourier transform infrared spectrophotometer (Bruker, Germany) with an ATR reflection module.[49] The plant sample was placed on the platform under uniform pressure and the spectra recorded involved sample scans of 32 scans with a resolution of 4 cm^{-1}. FTIR spectra of samples were recorded between 500 and 4000 cm^{-1}. The FTIR spectrophotometer was used to record the peaks.

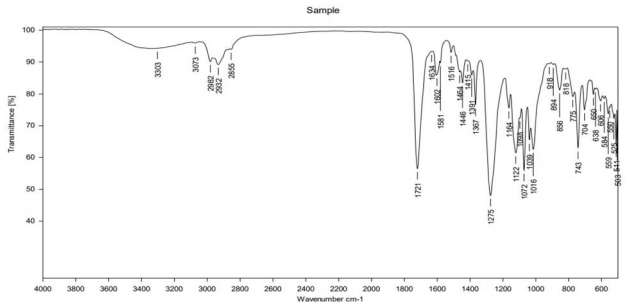

Fig. 4 The FTIR spectrum of *V. negundo* leaf extract obtained in the wavenumber range of 4000–500 cm^{-1}.

The functional groups in the plant extract from *V. negundo* were determined using FTIR analysis. The –OH stretching is represented by a peak at 3303 cm^{-1}, which denotes the presence of an alcoholic functional group. The amide group is indicated by a peak at 3073 cm^{-1}, which reflects –NH stretching. Peaks at 2982, 2932, and 2855 cm^{-1} signify the stretching of –CH. The carbonyl group is indicated by a peak at 1721 cm^{-1}, which represents stretching of –C═O. The aromatic group is indicated by peaks at 1415, 1446, 1464, 1516, and 1581 cm^{-1}, which represent –C═C stretching. –N–O is represented by peaks at 1367 and 1391 cm^{-1}.

The stretching of –C–O shown by a peak at 1275 cm^{-1} corresponds to an acid group. Peaks at 1164, 1122, 1098, 1072, 1039, and 1016 cm^{-1} show the presence of an ether group and represent –C–O stretching. Peaks at 918, 894, 856, and 818 cm^{-1} represent alkane C–H groups. Peaks at 775, 743, 704, 650, 638,

Table 2 The characteristic FTIR peaks identified in the ethanolic extract of a *Vitex negundo* plant sample

S. no.	Related functional group	Characteristics vibration (cm^{-1})	FTIR frequencies observed (IR_{max} in cm^{-1})
1	–OH (alcohol)	3200–3600	3303 cm^{-1}
2	–NH (amide)	3000–3300	3073 cm^{-1}
3	–CH	2850–3000	2982, 2932, 2855 cm^{-1}
4	–C═O (carbonyl)	1670–1820	1721 cm^{-1}
5	–C═C (aromatic)	10	1415, 1446, 1464, 1516, 1581 cm^{-1}
6	–N–O (nitro compound)	1320–1400	1367, 1391 cm^{-1}
7	–C–O (acid)	1210–1320	1275 cm^{-1}
8	–C–O (ether)	1000–1200	1164, 1122, 1098, 1072, 1039, 1016 cm^{-1}
9	C–H (alkanes)	800–1000	918, 894, 856, 818 cm^{-1}
10	C–H (aromatic)	600–800	775, 743, 704, 650, 638, 606 cm^{-1}
11	C–H (alkynes)	500–600	584, 559, 550, 525, 511, 503 cm^{-1}

and 606 cm^{-1} represent aromatic C–H groups. Alkyne C–H groups are defined by peaks at 584, 559, 550, 525, 511, and 503 cm^{-1}, as displayed in Fig. 4. The characteristic FTIR peaks identified in the ethanolic extract of the *Vitex negundo* plant sample are represented in Table 2.

The peaks in the FTIR spectrum confirmed the presence of phenols, flavonoids, carboxylic acids, primary amines, benzenes, nitro compounds, esters, ethers, and aromatic compounds in the *V. negundo* plant sample.

2.1.3.6 DFT studies. DFT[50,51] is one of the efficient quantum chemical computational approaches needed to research the characteristics of molecules and atoms in their ground states. It aids in comprehending the quantum chemical features of many different substances, including chemical reactivity, molecular structure, ionization potential, electron affinity, and many more.[52–54] In the current work, the 6-31G basis set and B3LYP level of theory[55] were used for all calculations.[56,57] The Gaussian 09 quantum chemistry package[58] was used for computations in the current investigation. The geometrically optimized structures of artemetin and catechin with the numbering of atoms are presented in Fig. 5.

3 Results and discussion

Phytochemical Screening: In the present study, the phytochemicals extracted from the leaves of the *Vitex negundo* plant in ethanol solvent exhibited a wide range of phytocompounds with bioactive properties.

Chemical composition: the principle of LC-MS analysis is to separate the individual components present in a solvent mixture by ionization and then analyse them based on their mass-to-charge ratio.[59] The chemical composition of the *V. negundo* leaf extract was determined using LC-MS analysis. The chromatograms of leaf extracts from *V. negundo* obtained using LC-MS investigations in both positive and negative ion modes are presented in Fig. 2 and 3. Based on LC-MS analysis, various phytochemicals with essential bioactive properties were obtained. Among these, artemetin and catechin, known for their anticancer properties, were further analysed by molecular docking and DFT studies against breast cancer targets.

3.1 Quantum chemical studies

3.1.1 Optimized geometrical analysis of artemetin and catechin. The geometrical optimization of the compounds artemetin and catechin was carried out using the B3LYP level of theory and 6-31G basis set.[54,55] These structures correspond to a true energy minimum on the potential energy surfaces, which indicates the absence of imaginary frequencies in these compounds.[60,61] The optimized molecular structures of artemetin and catechin obtained using the B3LYP level of theory and 6-31G basis set, with the atom numbering, are displayed in Fig. 5. The dihedral angle of artemetin is 24.141° (C19–C11–C6–C5) and the dipole moment is 5.8669 D. The dihedral angle of catechin is 48.099° (O6–C7–C8 C15) and the dipole moment is 2.2013 D. The dipole moment of molecules indicates electron density and polarizability, contributing significantly to the understanding of both intermolecular and intramolecular interactions, which is essential for predicting bulk and molecular properties.[62] The dipole moment of the catechin is higher than that of artemetin, contributing to its greater polarizability and higher electron density. The dihedral angle of catechin is higher compared to that of artemetin, indicating the higher stability of catechin (Fig. 5).

3.1.2 Frontier molecular orbital (FMO) theory. Frontier molecular orbital (FMO) theory[63] is used to assess the reaction stability of compounds. The frontier molecular orbitals determined for artemetin and catechin compounds at the B3LYP level of theory and using the 6-31G basis set are shown in Fig. 6. The highest occupied molecular orbital (HOMO) and lowest unoccupied molecular orbital (LUMO) energies of artemetin and catechin compounds were examined using FMO theory. The energy gap between the HOMO and LUMO indicates the relative stability of a compound. A larger energy gap indicates greater stability, while a smaller energy gap indicates lower stability.[61,64,65] Compounds with higher stability have lower chemical reactivity, while a smaller energy gap indicates

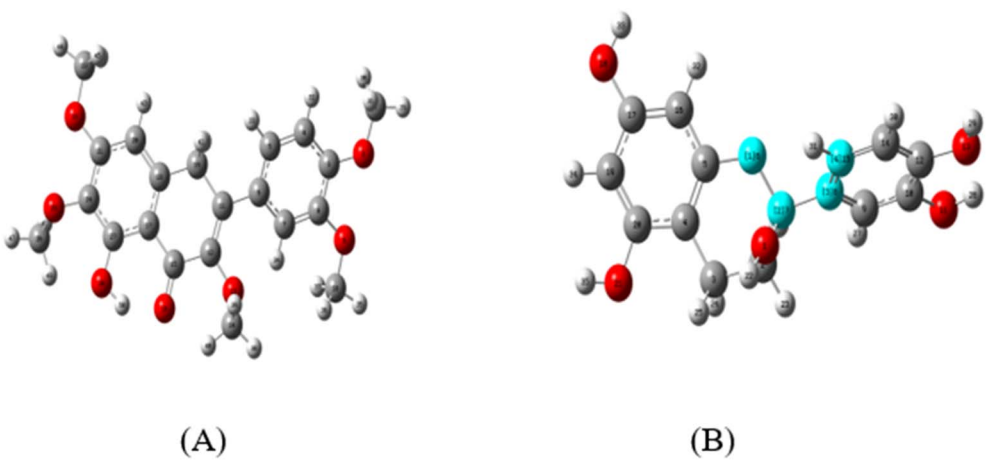

Fig. 5 The geometrically optimized structures of compounds with the numbering of atoms: (A) artemetin and (B) catechin.

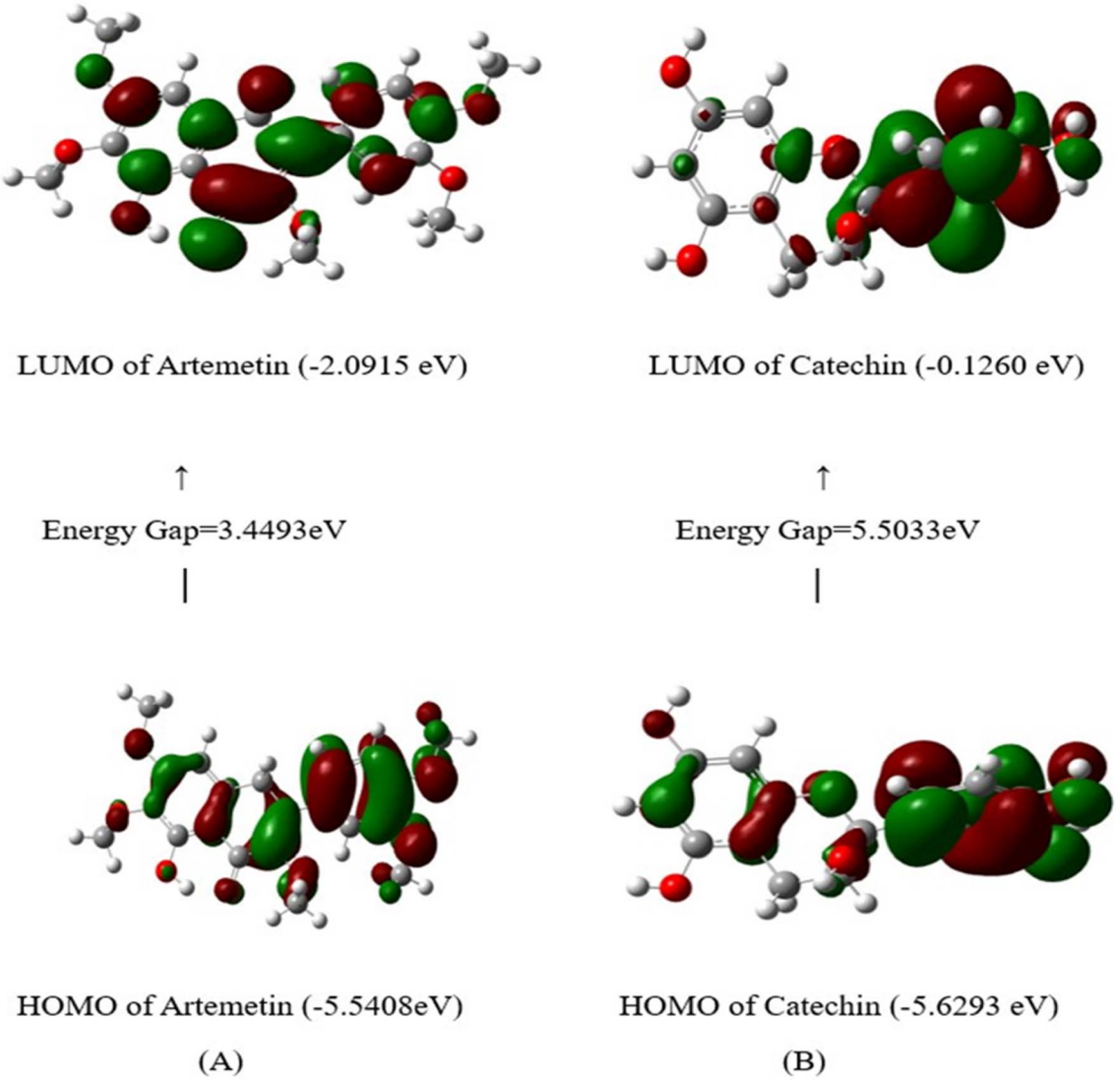

Fig. 6 FMO energies of (A) artemetin and (B) catechin; the positive phase is shown in red and the negative phase is shown in green.

a compound with higher chemical reactivity. Therefore, the smaller the energy gap between the HOMO and LUMO, the more likely an eventual electron transition and the lower the stability of a compound. Energy gaps are an essential parameter in analysing the electron conductivity.[66,67] HOMO–LUMO dissolution is the result of a considerable degree of intermolecular charge shifting from the electron donor group to the electron acceptor group. The areas of highest electron density of a molecule can be identified using the HOMO and LUMO. The chemical hardness of a molecule can also be used to analyze the chemical stability of a molecule. In the current study, the HOMO and LUMO energy differences for artemetin and catechin are 3.4493 eV and 5.5033 eV, respectively. Catechin has a larger energy gap than artemetin, exhibiting higher stability and lower chemical reactivity.

3.1.3 Molecular electrostatic potential (MEP) surface. The MEP surface63 distribution helps in understanding the size and shape of a molecule, which in turn reveals the regions of positive, negative, and neutral electrostatic potential, as well as the nature of its chemical bonds. The MEP surface is a necessary tool for the prediction of electrophilic and nucleophilic interactions of drugs.[67] The colour gradient on the MEP surface represents the molecular electrostatic potential. The electrostatic potentials over the compound surfaces are depicted in Fig. 7 with various colours. The red region signifies a more negative area characterized by low electrostatic potential, suggesting a surplus of electrons. Conversely, the blue region denotes a more positive region with elevated electrostatic potential, indicating a relative lack of electrons. It is clear that the electrical nature affects the shape and size of the molecules. The orientation of molecules with electrostatic potential also changes depending on the compounds.[65] Artemetin and catechin have a positive and negative region relating to C=O on the benzene ring. Electron density values are represented in increasing order as follows: red > yellow > green > blue.

The MEP surface of artemetin has a colour code that ranges from -7.504×10^{-2} (deep red, indicating an abundance of electrons) to 7.504×10^{-2} (dark blue, signifying a region of

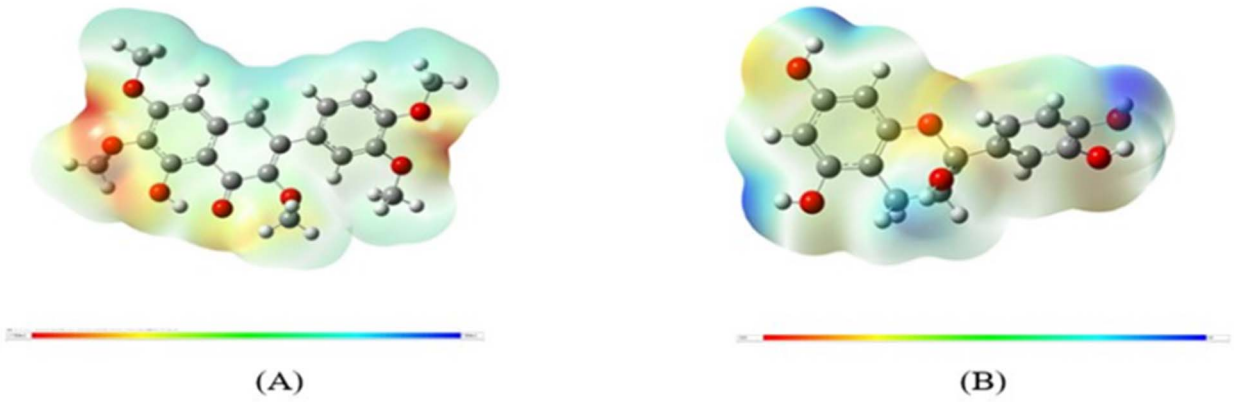

Fig. 7 Electron density surface maps of (A) artemetin and (B) catechin showing the electrostatic potentials of the respective molecules.

lower electron density). The MEP surface of catechin has a colour code that ranges from −0.0 (red, signifying an abundance of electrons) to 0.0 (deep blue, signifying a notable lack of electrons). According to the calculated MEP surface, red represents negative regions, which undergo electrophilic attack, and blue represents positive regions, which undergo nucleophilic attack in both the compounds. The MEP surface is coloured according to the following scheme: regions with a lack of electrons or partially positive regions are shown in blue; electron-rich and partially negative regions in red; slightly electron-rich regions in yellow; slightly electron-deficient regions in light blue; and neutral regions in green.[65,67]

3.1.4 Calculation of ionization potential, electron affinity and chemical potential values of the molecules. To study the stability of compounds, ionization potential (IP) and electron affinity (EA), the FMO, and HOMO–LUMO energy gaps were used as key parameters. Our findings show that compounds with higher IP and lower EA values are considerably more stable than those with lower IP and higher EA values (see Table 3). The chemical potential (μ), representing an electron's propensity to vanish from a molecule in its stable state, can be computed using the IP and EA values.[67]

The equations which relate the HOMO energy to the IP and the LUMO energy to the EA, in accordance with molecular orbital theory, are:

$$\mathrm{IP} = -E_{\mathrm{HOMO}};$$

$$\mathrm{EA} = -E_{\mathrm{LUMO}};$$

$$\text{Molecular chemical potential } (\mu) = -(\mathrm{IP} + \mathrm{EA})/2$$

3.1.5 Calculation of hardness (η) and softness (S) of the compounds. The charge-transfer resistance is primarily determined by the chemical hardness (η) and softness (S), which are inversely related to one another for a given chemical compound. The following equations were used based on molecular orbital theory to calculate compound hardness and softness:

$$\text{Hardness } (\eta) \text{ of the compound} = (\mathrm{IP} - -\mathrm{EA})/2$$

$$\text{Softness } (S) \text{ of the compound} = 1/\eta$$

The hardness and softness values for artemetin and catechin are calculated and represented in Table 3. A compound has its highest hardness in the steady state and its lowest hardness in the transition state, based on the principle of maximum hardness (PMH).[61] As a result, we found that catechin is harder than artemetin (see Table 3), which is consistent with their relative stabilities.[64,67]

According to Table 3, catechin is chemically more stable than artemetin, which is consistent with earlier findings (FMO and HOMO–LUMO energy gap). Under equilibrium conditions, artemetin has a greater tendency to lose electrons than catechin.

Table 3 HOMO, LUMO, HOMO–LUMO energy gap, IP, EA, chemical potential, hardness (η) and softness (S) values of the compounds (A) artemetin and (B) catechin

	6-31G basis set and B3LYP level of theory	
Molecular properties	(A) Artemetin	(B) Catechin
E_{HOMO} (eV)	−5.5408	−5.6293
E_{LUMO} (eV)	−2.0915	−0.1260
$E_{\mathrm{HOMO}} - E_{\mathrm{LUMO}}$ gap (eV)	3.4493	5.5033
Ionization potential (IP) (eV)	5.5408	5.6293
EA (eV)	2.0915	0.1260
Chemical potential (μ)	−3.8161	−2.8776
Hardness (η)	1.7246	2.7516
Softness (S)	0.5813	0.3636

3.2 QSAR modelling

The Cloud 3D-QSAR server[68] was employed to analyse the activity levels of phytochemicals along with their chemical structures.[34] A number of molecules chosen from the input molecules were provided as a test set, along with the test set proportion. After the successful QSAR run, we retrieved the results using various result visualization methods. The results of Cloud 3D-QSAR were obtained in tabular format, showcasing the top-ranked models, which included values for r^2, q^2, and r^2

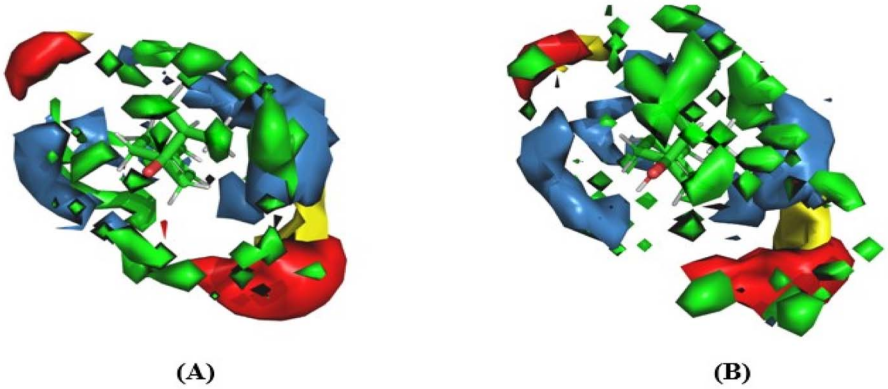

Fig. 8 Molecular force field contour plot from test sets: (A) artemetin and (B) catechin molecules. The green region indicates a rise in steric hindrance, causing increasing activity. The yellow region indicates the lowering of steric hindrance, causing decreasing activity. The blue region indicates that increasing the charge group helps to increase the activity. The red region indicates that increasing the charge group causes harmful effects to the activity.

Table 4 Linear regression data including training and test sets

Molecule name	Type	Experimental activity	Predictive activity	Residual[a]
Terpineol	Training	−2.371	−2.371	0.0000
Epicatechin	Training	−2.72	−3.2398	0.5198
Quercetin	Training	−4.024	17.1871	−21.2111
Casticin	Training	−4.077	−4.077	0.0000
Valencene	Training	−5.553	−5.553	0.0000
Catechin	Test	−3.092	−3.092	0.0000
Artemetin	Test	−4.397	−63.9069	59.5099

[a] Residual value = experimental value − predictive value.

predicted (refer to ESI Table 1†), as well as all models that were prioritized by the algorithm. The most effective QSAR models are represented by greater r^2, q^2, and r^2 predicted values. The biological activity was correlated positively or negatively with the steric bulk areas, represented by green/yellow contours, and the biological activity was correlated with negatively charged/hydrogen bond acceptor or positively charged/hydrogen bond donor substituent areas, represented by red/blue contours. This information is shown *via* molecular force field contour plots for individual models (see Fig. 8). Furthermore, a 3D representation of the aligned compounds was supplied. Based on the above-mentioned results, we validated the QSAR model and the molecular alignment. We also obtained comprehensive experimental values, predicted values, and residuals for each compound from this QSAR model.[68] We generated linear regression plots using this data (see Table 4 and Fig. 9). Based on this information, we can robustly estimate the activity of the relevant phytochemicals and their efficacy. Based on the residual values, we can conclude that terpineol, epicatechin, casticin, and valencene from the training data set and catechin from the test set have reliable correlation with the experimentally derived anticancer activities of the phytochemical compounds considered in this study.

The CoMFA QSAR equation is summarized graphically as a 3D contour map, showing fields such as steric, electrostatic, hydrophobic, and hydrogen bond accepting or donating fields, in which lattice points are associated with extreme values.

Molecular force field contour plots from the test sets are shown for artemetin and catechin molecules in Fig. 8a and b,

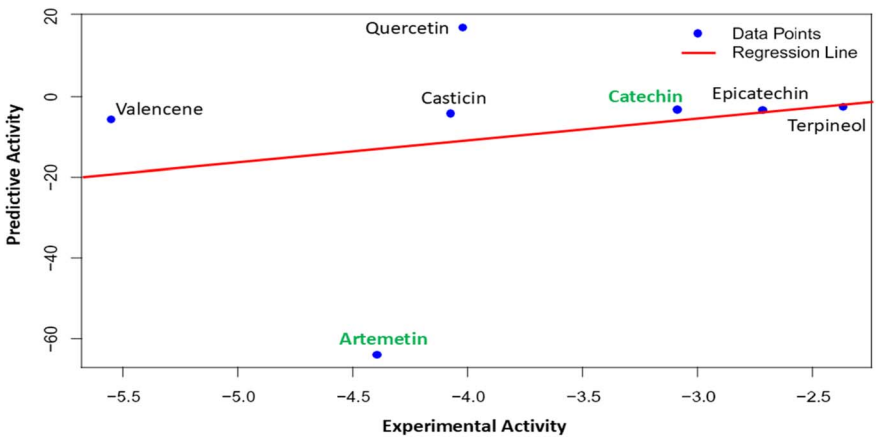

Fig. 9 A linear regression scatter plot of experimental activity *vs.* predictive activity of the compounds. The test compounds catechin and artemetin are highlighted in green.

Table 5 The binding energies of selected phytochemicals *versus* the breast cancer target protein

Ligand	HER2 (3RCD)
Artemetin	−7.3 kcal mol^{-1}
Catechin	−8.0 kcal mol^{-1}

respectively. An increase in steric hindrance is conducive to increasing the activity in places represented by the green area. A decrease in steric hindrance does not significantly improve the activity in places represented by the yellow area; intensifying the charge group helps increase the activity in places shown by the blue area, while areas where the charge group is harmful to the activity are indicated in red.

3.3 Molecular docking studies of phytochemicals

To analyze the binding modes of the queried ligands with a specific protein target, molecular docking simulations were carried out using Auto Dock Vina.[69,70] The selected phytocompounds from LC-MS analysis were docked with the anti-breast cancer target HER2 (PDB ID: 3RCD). Among seventeen phytocompounds docked against HER2, catechin and artemetin ligands selected after QSAR analysis showed higher affinity and more favorable binding energy scores, *i.e.* −8.0 kcal mol^{-1} and −7.3 kcal mol^{-1}, respectively, as shown in Table 5. For the post-docking analysis, PyMol[32] and Discovery Studio Visualizer[33] were employed to assess the bonding orientation between the ligands and the protein target. Artemetin displayed three C–H bonds: LEU-796, ARG-849 and PHE-864; one pi–anion bond: ASP-863; and seven pi–alkyl bonds: LEU-726, ALA-751, VAL-734, MET-774, LEU-785, LYS-753 and LEU-852. Catechin exhibited two conventional H-bonds: LEU-796 (2.3 Å) and MET-801 (2.5 Å); two pi–sigma bonds: THR-798 and LEU-852; and three pi–alkyl bonds: VAL-734, ALA-751 and LYS-753 (see Fig. 10 and 11).

According to earlier studies,[71,72] a lower binding energy score signifies a higher degree of ligand–protein bond stability. Among the phytocompounds, the ones that formed the best

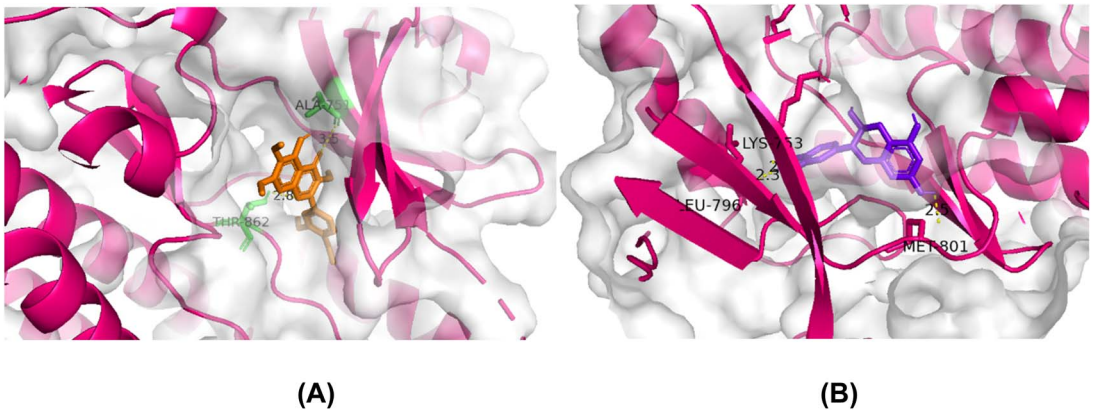

Fig. 10 A depiction of the 3D molecular docking interactions of HER2 with the ligands (A) catechin and (B) artemetin.

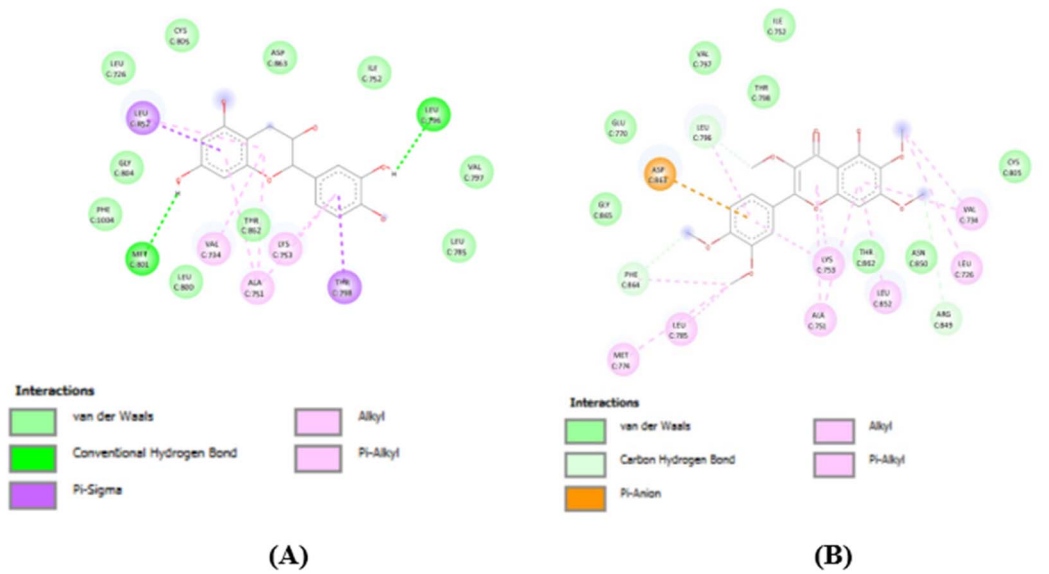

Fig. 11 2D plots of the interactions of surrounding HER2 amino acids with (A) catechin and (B) artemetin.

ligand–protein conformations with the breast cancer protein targets were artemetin and catechin. Grading of the molecular docking analysis of artemetin and catechin with the target protein was based on the binding energies and binding conformations obtained. The protein target HER2, which is the prime target for anti-breast cancer action, has a higher binding affinity for ligands than other proteins, according to the docking studies. The natural phytocompounds derived from *V. negundo*, artemetin and catechin, demonstrated consistent docking results.

4 Conclusions

In summary, we analysed the quantum chemical properties, quantitative structure activity relationships and docking potentials against an anti-breast cancer target using bioactive compounds extracted from *V. negundo* to prioritize them based on their anticancer activity and efficacy. Our study indicates that *V. negundo* extract shows antioxidant and anticancer properties. Based on FTIR analysis, the functional groups of the bioactive compounds were revealed. Further, DFT studies confirmed that in comparison to artemetin, catechin is more stable and less chemically reactive, as indicated by the HOMO and LUMO energy gaps and energy levels. The charge-transfer resistance of these bioactive compounds was determined based on the hardness (η) and softness (S). As a result, we found that catechin is harder than artemetin, which is consistent with their relative stabilities. These bioactive compounds were further screened using QSAR residual scores for their activity and molecular docking simulations to discover the binding modes of the ligands with an anti-breast cancer target (HER2). Artemetin and catechin showed favourable binding conformations with HER2 in the molecular docking simulations. Thus, by adopting this pipeline, target-specific anti-breast-cancer ligands with the highest binding affinities can be efficiently prioritized, allowing only the most promising molecules to be isolated and purified—steps that are otherwise time-consuming, labour-intensive, and costly. As mentioned above, the protocol is effective for screening and isolating potential compounds in less time and with improved cost-effectiveness as part of the drug discovery and development process.

Data availability

The data that support the findings of this study are available from the authors and will be provided upon reasonable requests.

Author contributions

Lakshmi B. S.: formal analysis, conceptualization, investigation, methodology, validation, visualization, writing – original draft. Jayanna B.: analysis, methodology, validation, visualization, editing & reviewing – original draft. Anil H. G.: data curation, software, visualization, reviewing – original draft. Ravindranath B. S.: conceptualization, investigation, methodology, analysis, software, validation, visualization, editing and reviewing – original draft.

Conflicts of interest

There are no conflicts to declare.

Acknowledgements

Authors would like to express their sincere gratitude to BNM Institute of Technology, Bangalore and Manipal Institute of Technology, MAHE, Manipal for providing the resources and the funds for the current research work.

Notes and references

1 M. A. Ashraf, Phytochemicals as potential anticancer drugs: time to ponder nature's bounty, *Biomed Res. Int.*, 2020, **7**, 2020, DOI: **10.1155/2020/8602879**.

2 B. Rizeq, I. Gupta, J. Ilesanmi, M. AlSafran, M. M. Rahman and A. Ouhtit, The power of phytochemicals combination in cancer chemoprevention, *J. Cancer*, 2020, **11**, 4521–4533, DOI: **10.7150/jca.34374**.

3 M. Shanwaz Mohammad and P. Shyam, *J. Mol. Struct.*, 2023, **1288**, 135762, DOI: **10.1016/j.molstruc.2023.135762**.

4 B. Kaushik, J. Sharma, P. Kumar and A. Shourie, Phytochemical properties and pharmacological role of plants: secondary metabolites, *Biosci., Biotechnol. Res. Asia*, 2021, **18**, 23–35, DOI: **10.13005/bbra/2894**.

5 H. T. Ly, T. M. Truong, T. T. Nguyen, H. D. Nguyen, Y. Zhao and V. M. Le, Phytochemical screening and anticancer activity of the aerial parts extract of Xanthium strumarium L. on HepG2 cancer cell line, *Clin. Phytosci.*, 2021, **7**, 1–8, DOI: **10.1186/s40816-021-00252-w**.

6 S. G. Balraj, M. Richa, Navgeet and S. Kumar, *Mol. Biol. Rep.*, 2018, **45**, 2925–2934, DOI: **10.1007/s11033-018-4421-3**.

7 B. Neha, R. Jannavi and P. Sukumaran, Phyto-pharmacological and biological aspects of vitex negundo medicinal plant-A review, *Cardiovasc. Disord.*, 2021, **6**(7), 17–32, DOI: **10.9734/JPRI/2021/v33i29A31562**.

8 N. Kamal, N. S. Mio Asni, I. N. Rozlan, M. A. Mohd Azmi, N. W. Mazlan, A. Mediani, S. N. Baharum, J. Latip, S. Assaw and R. A. Edrada-Ebel, Traditional medicinal uses, phytochemistry, biological properties, and health applications of Vitex sp, *Plants*, 2022, **11**, 1944, DOI: **10.3390/plants11151944**.

9 M. Kumar Dwivedi, R. Shukla, N. K. Sharma, A. Manhas, K. Srivastava, N. Kumar and P. K. Singh, *J. Ethnopharmacol.*, 2021, **275**, 114076, DOI: **10.1016/j.jep.2021.114076**.

10 C. K. Swaliha, P. Krishnakumar, M. Rupa, N. Premanand, C. Kalaiselvan, S. Nanda Kumar and M. Surendra Kumar, *World J. Pharm. Res.*, 2022, **11**(4), 780–791, DOI: **10.20959/wjpr20224-23615**.

11 N. Koirala, C. Dhakal, N. Narayan Munankarmi, S. W. Ali, A. Hameed, N. Martins, J. Sharifi-Rad, M. Imran, A. M. Arif, M. S. Hanif, R. Chandra Basnyat and B. Salehi,

Cell. Mol. Biol., 2020, **66**(4), 1–7, DOI: **10.14715/cmb/2020.66.4.1**.

12 F. Bray, M. Laversanne, H. Sung, J. Ferlay, R. L. Siegel, I. Soerjomataram and A. Jemal, Global cancer statistics 2022: GLOBOCAN estimates of incidence and mortality worldwide for 36 cancers in 185 countries, *Ca-Cancer J. Clin.*, 2024, **74**, 229–263.

13 A. N. Giaquinto, H. Sung, K. D. Miller, J. L. Kramer, L. A. Newman, A. Minihan, A. Jemal and R. L. Siegel, Breast cancer statistics, 2022, *Ca-Cancer J. Clin.*, 2022, **72**(6), 524–541, DOI: **10.3322/caac.21754**.

14 J. Wang, T. Han, B. Hou, P. Zhang, W. Qi, B.-L. Zhang, Y.-W. Huang, Y. Wang, Z.-M. Xiang and C.-T. Zi, Xuan-Jun Wang and Jun Sheng, *RSC Adv.*, 2017, **7**, 54136, DOI: **10.1039/C7RA11496F**.

15 R. Acharya, S. Chacko, P. Bose, A. Lapenna and S. Prasad Pattanayak, *Sci. Rep.*, 2019, **9**, 15743, DOI: **10.1038/s41598-019-52162-0**.

16 A. Giró-Perafita, S. Palomeras, D. H. Lum, A. Blancafort, G. Viñas, G. Oliveras, F. Pérez-Bueno, A. Sarrats, A. L. Welm and T. Puig, Preclinical evaluation of fatty acid synthase and EGFR inhibition in triple-negative breast cancer, *Clin. Cancer Res.*, 2016, **22**(18), 4687–4697, DOI: **10.1158/1078-0432.CCR-15-3133**.

17 R. Danesi, S. Fogli, S. Indraccolo, M. Del Re, A. P. Dei Tos, L. Leoncini, L. Antonuzzo, L. Bonanno, V. Guarneri, A. Pierini, G. Amunni and P. Conte, *ESMO Open*, 2021, **6**, 2, DOI: **10.1016/j.esmoop.2020.100040**.

18 R. Hong and B. Xu, *Cancer Commun.*, 2022, **42**, 913–936, DOI: **10.1002/cac2.12358**.

19 E. BarrettConnor, L. Mosca, P. Collins, M. J. Geiger, D. Grady, M. Kornitzer, M. A. McNabb and N. K. Wenger, *N. Engl. J. Med.*, 2006, **355**, 125–137, DOI: **10.1056/NEJMoa062462**.

20 V. Shrihastini, P. Muthuramalingam, S. Adarshan, M. Sujitha, J.-T. Chen, H. Shin and M. Ramesh, *Cancers*, 2021, **13**(24), 6222, DOI: **10.3390/cancers13246222**.

21 V. Nguyen, M. Espiritu and F. Elbarbry, *Biomed. Chromatogr.*, 2020, **34**(3), e4789, DOI: **10.1002/bmc.4789**.

22 O. Ousji and L. Sleno, *Antioxidants*, 2022, **11**, 1635, DOI: **10.3390/antiox11091635**.

23 S. Wang, T. Cai, H. Liu, A. Yang and J. Xing, *J. Sep. Sci.*, 2019, 3277–3390, DOI: **10.1002/jssc.201900668**.

24 V. K. Singh, H. Chaurasia, R. Mishra, R. Srivastava, N. Farha, P. Kumar and R. K. Singh, *J. Mol. Struct.*, 2022, **1247**, 131400, DOI: **10.1016/j.molstruc.2021.131400**.

25 Y.-L. Wang, F. Wang, X.-X. Shi, C.-Y. Jia, F.-X. Wu, H. Ge-Fei and G.-F. Yang, *Briefings Bioinf.*, 2021, **22**(4), 1–8, DOI: **10.1093/bib/bbaa276**.

26 M. A. Salem, L. Perez de Souza, S. Ahmed, A. R. Fernie, M. A. Farag, S. M. Ezzat and S. Alseekh, *Metabolites*, 2020, **10**, 37, DOI: **10.3390/metabo10010037**.

27 M. Ranjan Sahoo and M. Srinivasan Umashankara, *Pharmacogn. Res.*, 2023, **15**(1), 163–167, DOI: **10.5530/097484900288**.

28 S. V. Taralkar and S. Chattopadhyay, *J. Anal. Bioanal. Tech.*, 2012, **3**, 1–6, DOI: **10.4172/2155-9872.1000134**.

29 Q.-Y. Gai, J. Jiao, X. Wang, Y. -J. Fu, L. Yao, J. Liu, Z.-Y. Wang and X.-J. Xu, *Food Chem.*, 2021, **335**, 127602, DOI: **10.1016/j.foodchem.2020.127602**.

30 E. Israel Edache, A. Uzairu, P. Andrew Mamza and G. Adamu Shallangwa, *Sci. Afr.*, 2022, **15**, e01088, DOI: **10.1016/j.sciaf.2021.e01088**.

31 P. Tosco, T. Balle and F. Shiri, Open3DALIGN: an open-source software aimed at unsupervised ligand alignment, *J. Comput.-Aided Mol. Des.*, 2011, **25**, 777–783, DOI: **10.1007/s10822-011-9462-9**.

32 S. Yuan, H. S. Chan and Z. Hu, Using PyMOL as a platform for computational drug design, *Wiley Interdiscip. Rev.: Comput. Mol. Sci.*, 2017, **7**(2), e1298, DOI: **10.1002/wcms.1298**.

33 D. S. Visualizer, *Discovery Studio Visualizer. 2*, Accelrys software inc., 2005.

34 Y. L. Wang, F. Wang, X. X. Shi, C. Y. Jia, F. X. Wu, G. F. Hao and G. F. Yang, Cloud 3D-QSAR: a web tool for the development of quantitative structure–activity relationship models in drug discovery, *Briefings Bioinf.*, 2021, **22**(4), bbaa276, DOI: **10.1093/bib/bbaa276**.

35 M. Chartier and R. Najmanovich, Detection of binding site molecular interaction field similarities, *J. Chem. Inf. Model.*, 2015, **55**(8), 1600–1615, DOI: **10.1021/acs.jcim.5b00333**.

36 G. Van Vo, T.-H.-T. Nguyen, T.-P. Nguyen, T.-H.-T. Do, N.-M. A. Tran, H. T. Nguyen and T. T. Nguyen, *Saudi Pharm. J.*, 2022, **30**, 1301–1314, DOI: **10.1016/j.jsps.2022.06.018**.

37 S. K. Burley, C. Bhikadiya, C. Bi, S. Bittrich, H. Chao, L. Chen, P. A. Craig, G. V. Crichlow, K. Dalenberg, J. M. Duarte and S. Dutta, RCSB Protein Data Bank (RCSB. org): delivery of experimentally-determined PDB structures alongside one million computed structure models of proteins from artificial intelligence/machine learning, *Nucleic Acids Res.*, 2023, **51**(D1), D488–D508, DOI: **10.1093/nar/gkac1077**.

38 S. K. Burley, C. Bhikadiya, C. Bi, S. Bittrich, H. Chao, L. Chen, P. A. Craig, G. V. Crichlow, K. Dalenberg, J. M. Duarte and S. Dutta, *Nucleic Acids Res.*, 2023, **51**(D1), D488–D508, DOI: **10.1093/nar/gkac1077**.

39 F. A. Kolpakov and V. N. Babenko, *Mol. Biol.*, 1997, **31**, 540–547.

40 S. Dallakyan and A. J. Olson, *Chemical Biology: Methods and Protocols*, 2015, pp. 243–250.

41 G. M. Morris, R. Huey, W. Lindstrom, M. F. Sanner, R. K. Belew, D. S. Goodsell and A. J. Olson, *J. Comput. Chem.*, 2009, **30**, 2785–2791, DOI: **10.1002/jcc.21256**.

42 S. Kim, J. Chen, T. Cheng, A. Gindulyte, J. He, S. He, Q. Li, B. A. Shoemaker, P. A. Thiessen, B. Yu and L. Zaslavsky, PubChem 2019 update: improved access to chemical data, *Nucleic Acids Res.*, 2019, **47**(D1), D1102–D1109, DOI: **10.1093/nar/gky1033**.

43 N. M. O'Boyle, M. Banck, C. A. James, C. Morley, T. Vandermeersch and G. R. Hutchison, Open Babel: An open chemical toolbox, *J. Cheminf.*, 2011, **3**, 1–4, DOI: **10.1186/1758-2946-3-33**.

44 S. Yuan, H. C. Stephen Chan and Z. Hu, *WIREs Comput. Mol. Sci.*, 2017, e1298, DOI: **10.1002/wcms.1298**.

45 S. Kim, Exploring chemical information in PubChem, *Curr. Protocol.*, 2021, **1**, e217, DOI: 10.1002/cpz1.217.
46 S. Sharma, A. Sharma and U. Gupta, *Ann. Antivir. Antiretrovir.*, 2021, **5**(1), 028–032, DOI: 10.17352/aaa.000013.
47 B. Ahmad Bhat, W. Rashid Mir, A. S. Bashir, M. Alkanani and M. Ahmad Mir, *Sci. Rep.*, 2022, **12**, 7296, DOI: 10.1038/s41598-022-10796-7.
48 A. Ricci, K. J. Olejar, G. P. Parpinello, P. A. Kilmartin and A. Versari, Application of Fourier transform infrared (FTIR) spectroscopy in the characterization of tannins, *Appl. Spectrosc. Rev.*, 2015, **50**, 407–442, DOI: 10.1080/05704928.2014.1000461.
49 S. Luo, J. Tian, Z. Liu, Q. Lu, K. Zhong and Xu Yang, *Measurement*, 2019, 0263–2241, DOI: 10.1016/j.measurement.2019.107204.
50 A. Elmi, S. M. Ahmed, N. Siddiqui, S. Al Jawad, M. Nour, I. Miganeh and S. Javed, *J. Drug Delivery Ther.*, 2021, **11**(1-s), 71–82, DOI: 10.22270/jddt.v11i1-s.4702.
51 A. E. M. Abdallah, S. A. Abdel-Latif and G. H. Elgemeie, Novel Fluorescent Benzothiazolyl-Coumarin Hybrids as Anti-SARSCOVID-2 Agents Supported by Molecular Docking Studies: Design, Synthesis, X-ray Crystal Structures, DFT, and TD-DFT/PCM Calculations, *ACS Omega*, 2023, **8**, 19587–19602, DOI: 10.1021/acsomega.3c01085.
52 W. Kohn and L. Sham, Density functional theory, in *Conference Proceedings-Italian Physical Society*, Editrice Compositori, 1996, vol. 49, pp. 561–572.
53 F. M. Bickelhaupt and E. J. Baerends, Kohn-Sham density functional theory: predicting and understanding chemistry, *Rev. Comput. Chem.*, 2000, **1**, 1–86, DOI: 10.1002/9780470125922.
54 G. Seifert, Tight-binding density functional theory: an approximate Kohn− Sham DFT scheme, *J. Phys. Chem. A*, 2007, **111**(26), 5609–5613, DOI: 10.1021/jp069056r.
55 A. V. Mitin, J. Baker and P. Pulay, An improved 6-31G* basis set for first-row transition metals, *J. Chem. Phys.*, 2003, **118**(17), 7775–7782, DOI: 10.1063/1.1563619.
56 M. Lozynski, D. Rusinska-Roszak and H. G. Mack, Hydrogen bonding and density functional calculations: The B3LYP approach as the shortest way to MP2 results, *J. Phys. Chem. A*, 1998, **102**(17), 2899–2903, DOI: 10.1021/jp973142x.
57 H. Kruse, L. Goerigk and S. Grimme, Why the standard B3LYP/6-31G* model chemistry should not be used in DFT calculations of molecular thermochemistry: understanding and correcting the problem, *J. Org. Chem.*, 2012, **77**(23), 10824–10834, DOI: 10.1021/jo302156p.
58 J. Singh, *Res. Chem. Intermed.*, 2020, **46**, 2457–2479, DOI: 10.1007/s11164-020-04101-2.
59 D. F. Tegegn, H. Z. Belachew and A. O. Salau, *Sci. Rep.*, 2024, **14**, 8146, DOI: 10.1038/s41598-024-58599-2.
60 M. Beccaria and D. Cabooter, *Analyst*, 2020, **145**, 1129–1157, DOI: 10.1039/C9AN02145K.
61 J. Deva Anban, C. James, J. Sharmi Kumar and S. Pradhan, *SN Appl. Sci.*, 2020, **2**, 1685, DOI: 10.1007/s42452-020-03493-5.
62 M. A. Mostafa, M. A. Ibrahim, S. S. Ibrahim, N. Mohamed and Al-S. Badran, Synthetic approaches for novel 3-heteroaryl-4-hydroxy-1-methylquinoline-2(1H) one:spectroscopic characterization, molecular dockingand DFT investigations, *RSC Adv.*, 2025, **15**, 6718, DOI: 10.1039/d5ra00325c.
63 S. Thiruvangoth, Exploring the spectral and nonlinear optical properties of phenyl isothiocyanate through density functional theory and molecular docking studies: A comprehensive analysis of a potent biologically active phytochemical, *Hybrid Adv.*, 2024, **6**, 100214, DOI: 10.1016/j.hybadv.2024.100214.
64 S. Chandrasekhar, H. R. Deepa, R. M. Melavanki, S. Mogurampelly, M. M. Basanagouda, S. Yallappa and J. Thipperudrappa, *Chem. Data Collect.*, 2020, **29**, 100516, DOI: 10.1016/j.cdc.2020.100516.
65 P. Vinduja, V. K. Rajan, S. Krishna and K. Muraleedharan, A Computational Modeling of the Structure, Frontier Molecular Orbital (FMO) Analysis, and Global and Local Reactive Descriptors of a Phytochemical 'Coumestrol, in *Mathematics Applied to Engineering in Action*, Apple Academic Press, 2021, vol. 21, pp. 41–60, DOI: 10.1201/9781003055174-2.
66 Y. Huang, C. Rong, R. Zhang and S. Liu, Evaluating frontier orbital energy and HOMO/LUMO gap with descriptors from density functional reactivity theory, *J. Mol. Model.*, 2017, **23**, 1–2, DOI: 10.1007/s00894-016-3175-x.
67 J. Wang, T. Han, B. Hou, P. Zhang, W. Qi, B.-L. Zhang, Y.-W. Huang, Y. Wang, Z.-M. Xiang, C.-T. Zi, X.-J. Wang and J. Sheng, *RSC Adv.*, 2017, **7**, 54136, DOI: 10.1039/C7RA11496F.
68 Danishuddin and A. U. Khan, *Drug Discovery Today*, 2016, **21**, 8, DOI: 10.1016/j.drudis.2016.06.013.
69 G. Van Vo, T.-H.-T. Nguyen, T.-P. Nguyen, T.-H.-T. Do, N.-M. A. Tran, H. T. Nguyen and T. T. Nguyen, *Saudi Pharm. J.*, 2022, **30**, 1301–1314, DOI: 10.1016/j.jsps.2022.06.018.
70 R. Patel, J. Prajapati, P. Rao, R. M. Rawal, M. Saraf and D. Goswami, *Mol. Diversity*, 2021, 1–21, DOI: 10.1007/s11030-021-10325-0.
71 A. K. Singh, S. K. Katari, A. Umamaheswari and A. Raj, *RSC Adv.*, 2021, **11**, 14632–14653, DOI: 10.1039/D0RA10840E.
72 N. S. Jangwan, M. Khan, R. Das, N. Altwaijry, A. M. Sultan, R. Khan, S. Saleem and M. F. Singh, *Front. Pharmacol*, 2024, **15**, 1366279, DOI: 10.3389/fphar.2024.1366279.